Available online at www.sciencedirect.com
SCIENCE DIRECT®
Journal of Magnetic Resonance 167 (2004) 12–24
JMR Journal of Magnetic Resonance
www.elsevier.com/locate/jmr

Communication

Image brightening in samples of high dielectric constant☆

James Tropp*

General Electric Medical Systems, 47697 Westinghouse Drive, Fremont, CA 94539, USA

Received 19 May 2003; revised 12 November 2003

Abstract

An analytic solution is given for the electromagnetic problem of a lossy dielectric cylinder of infinite length, irradiated by a circularly polarized radiofrequency (RF) magnetic field; the NMR-active components of the field inside the cylinder are projected out by transforming the RF Hamiltonian to the rotating frame and retaining only those terms independent of time; it is noted that the resulting cartesian field components are required to be real. The squared magnitude of the NMR-active fields are then used to calculate the gradient-recalled images of the cylinder, for small tip angles of the magnetization; and the result is shown to predict almost quantitatively the intensity patterns of experimental proton images at 3.0 and 4.0 T, in a cylindrical phantom of radius 9.25 cm, filled with 0.05 M aqueous NaCl. In particular, the artifactual brightening at the center of the recorded image is convincingly reproduced in a simulation, whose underlying model excludes wave propagation along the direction of the cylinder axis. Formation of the artifact is explained in terms of the focussing of the RF magnetic field at the center of the cylinder, as illustrated by contour plots showing the time evolution of the rotating flux. An extended electromagnetic model—having the dielectric cylinder enclosed in a long, shielded volume resonator (e.g., of bird cage type)—is then sketched. The mathematical details appear in Appendix A; and the simulated images are shown to be virtually indistinguishable from those of the simpler original model. The theory of the Q, or quality factor, of the dielectric cylinder—considered itself as a resonant object—is developed for the enclosed cylinder model, where flux containment by the shield permits an unambiguous treatment of both the stored energy and the radiative losses. This is extended to treat the Q of a lossy dielectric sphere without shielding. Further plots of flux contours are given for the sphere, excited at 208 MHz with a uniform circularly polarized field, as well as by a surface coil, and for the enclosed cylinder in the range 140–160 MHz. It is then argued that the center brightening artifacts in magnetic resonance images are due to the underdamped dielectric resonance of the sample, i.e., at $Q > 0.5$, while the overdamped condition, $Q < 0.5$, leads to exclusion of flux from the center, i.e., to the classic skin effect. The term 'dielectric resonance' is shown to require careful interpretation for mixed-mode excitation, such as occurs with a surface coil. An extended reciprocity formula for NMR reception, valid for an arbitrary electromagnetic Green's function, is also given in Appendix B.

1. Introduction

Many investigators, but Röschmann in particular [1–3], have called attention to an intensity artifact—typically brightening at the center—observed in magnetic resonance images of objects whose dimensions are comparable to the radiofrequency (RF) wavelength [4–11]. These distortions arise from focussing of the RF magnetic flux lines, and are attributed by Röschmann quite generally to dielectric resonance [2,3]. Although often suppressed by preferential saturation, the brightening artifacts (as we shall call them), are typically noticeable in proton images of the human head, acquired with volume resonators at static field strengths of 4.0 T and above; they are pronounced, even dramatic, at 7.0 T, where the Larmor frequency approaches 300 MHz [9]. Since radiofrequency propagation is strongly damped by the high conductivity typical of biological samples [11], the question has been raised, whether true resonances are in fact observed, and it has been has argued [8] that field focussing and dielectric resonance are not identical.

While Röschmann [2,3], has stressed the importance of the 'eigen-fields' of the irradiated dielectric body,

☆ A preliminary account of this work appeared in the Proceedings of International Society for Magnetic Resonance in Medicine, Denver, 2000.

* Fax: 1-510-656-4260.
E-mail address: james.tropp@med.ge.com.

1090-7807/$ - see front matter © 2003 Elsevier Inc. All rights reserved.
doi:10.1016/j.jmr.2003.11.003

other workers have emphasized its interaction with the irradiating resonator, and have proposed that cylindrical volume resonators may be designed to manipulate the axial propagation constant, and thereby improve RF homogeneity [4,5,7], effectively cancelling the artifact.

Here, we present examples of theoretical images with center brightening, calculated in the transaxial plane of a lossy dielectric cylinder, at 128 and 170 MHz. The calculations are based largely on the electromagnetic model of the cylinder in free space, used by Glover et al. in their seminal study of linear and quadrature excitation [12], and later elegantly reprised by Tofts [13]; the essentials are also given by Landau and Lifschitz [14]. Elaboration of this model, to include the presence of a shielded radiofrequency antenna (or probe) enclosing the dielectric, does not noticeably change the results. To select the proper components of the rotating RF field, we introduce a projection algorithm, based upon transformation of the RF Hamiltonian to the rotating frame. The calculations rigorously exclude axial propagation effects, and yet faithfully (almost quantitatively) reproduce the essential features of experimental images, recorded under the same conditions used in theory. While the results do not exclude the suppression of the brightening artifact by suitably designed excitation, they do appear to disallow a significant role for the axial propagation constant in cylindrical volume resonators.

We also present a series of calculations, showing how the RF flux contours inside a dielectric depend upon the Q or quality of factor of the specimen, itself considered as a resonant object. The enclosed dielectric model (vide supra) affords a rigorous development of the theory for the cylinder, due to spatial confinement of the scattered fields and the restriction of radiative losses to dissipation in the shield; a satisfactory theory is then given by analogy for the dielectric sphere, although in less compact form. Calculated flux contours are presented for the cylinder at in the range of 140–160 MHz, and for the sphere at 208 MHz. Our results support Röschmann's viewpoint that the brightening artifact is essentially diagnostic of true dielectric resonance, and that this appellation has significance beyond the purely semantic.

Finally, given the importance of the reciprocity principle [15–17] in this type of calculation, we append a brief derivation of the familiar Hoult–Richards formula, based upon an arbitrary Green's function, and therefore of quite general applicability, in the regimes of either long or short wavelength.

2. Theory

We consider a long, lossy, dielectric cylinder, with an alternating radiofrequency B_1 field, uniform at infinity, incident normal to the cylinder axis. The complex wavevector $\mathbf{k}$, inside the cylinder, is determined from:

$$\mathbf{k}^2 = \mathrm{i}\omega\mu_0\sigma + \omega^2\varepsilon\varepsilon_0\mu_0, \tag{1}$$

where σ is the conductivity (in Siemens/M), the free space permittivity and dielectric constants appear with the subscript zero, the unadorned ε is the relative dielectric constant, and ω is the angular frequency of the applied field. Then for a pair of linearly polarized excitation fields, applied along the x and y coordinate axes (and indexed by superscripts 1 and 2, for reasons which will emerge), the vector potentials of the response, inside the cylinder are:

$$\boldsymbol{A}^{(1)}(r,\phi) = -2\mathbf{e}_z B\frac{J_1(kr)\sin\phi}{kJ_0(ka)}, \tag{2}$$

$$\boldsymbol{A}^{(2)}(r,\phi) = -2\mathbf{e}_z B\frac{J_1(kr)\cos\phi}{kJ_0(ka)}, \tag{3}$$

where the Js are bessel functions (of order zero and one), a is the radius of the cylinder, r and ϕ are cylindrical polar coordinates, B is the strength of the exciting field component in the absence of the cylinder, and $\mathbf{e}_Z$ is the unit vector in the z direction. We will also make use of the corresponding vector potentials for a spherical phantom, subjected to the same incident fields as the cylinder:

$$\boldsymbol{A}^{(1)}(r,\vartheta) = \boldsymbol{\phi}\frac{3B}{2}\frac{\sin\vartheta\psi_1(kr)}{k\psi_0(ka)}, \tag{4}$$

$$\boldsymbol{A}^{(2)}(r,\vartheta) = \boldsymbol{\phi}'\frac{3B}{2}\frac{\cos\vartheta\psi_1(kr)}{k\psi_0(ka)}, \tag{5}$$

where the ψ_n are spherical bessel functions as given by Sommerfeld [18], r and θ are spherical coordinates, a is now the radius of the sphere, and $\boldsymbol{\phi}$ the conventional ϕ-directed unit vector in spherical coordinates, from which $\boldsymbol{\phi}'$ is obtained by a rotation of $\pi/2$ of the angle θ. While the underlying boundary value problem has been treated elsewhere in the NMR literature [2,8,19,20] the present formulae are obtained by transformation of Smythe's result for a conductive, permeable sphere [21]; i.e., Smythe uses $\mathbf{k}^2 = \mathrm{i}\omega\mu_0\sigma$, rather than our $\mathrm{i}\omega\mu_0\sigma + \omega^2\varepsilon\varepsilon_0\mu_0$ [cf. Eq. (1)].

Note that both sets of potentials, the cylindrical and the spherical, have denominators consisting of zero-order bessel functions whose arguments are the products of a wave vector and a radius. In the case of zero conductivity, the zeroes of the these bessel functions lie directly on the real axis; while as conductivity increases, they are progressively displaced along the imaginary axis; as such they may be said mathematically to constitute a series of resonant denominators, so that the dielectric samples may themselves be thought of as exhibiting resonant behavior, including, in the limit of high conductivity, over-damping.

For a pair of linear exciting fields, applied in space *and* time quadrature, so as to produce a positive sense

for the rotating field, the time-dependent vector potential of the response becomes:

$$\begin{aligned}\boldsymbol{A} &= \text{real}\{[\boldsymbol{A}^{(1)}(r,\phi) + i\boldsymbol{A}^{(2)}(r,\phi)]\exp i\omega t\} \\ &= [\boldsymbol{A}^{(1,\text{Re})} - \boldsymbol{A}^{(2,\text{Im})}]\cos\omega t - [\boldsymbol{A}^{(1,\text{Im})} + \boldsymbol{A}^{(2,\text{Re})}]\sin\omega t,\end{aligned} \tag{6}$$

where the superscripts 1 and 2 identify (as above) the source of excitation, and the real and imaginary components of the potentials are indicated with the additional superscripts, Re and Im. The time quadrature shift of $\boldsymbol{A}^{(2)}$ is provided by the factor i; and, inasmuch as the argument of the exponential is always positive by convention, the sense of the rotation is reversed by switching from i to $-i$; as in $\boldsymbol{A}^{(1)} \pm i\boldsymbol{A}^{(2)}$; the reversal does not require complex conjugation of the potentials (or their resulting fields. Finally, in free space, or at sufficiently low frequency, the quasi-static vector potential may be written in cartesian coordinates as

$$\boldsymbol{A}^{(\text{quasi})}(x,y) = \mathbf{e}_z B\text{Re}\{(y + \text{i}x)\exp\text{i}\omega t\}, \tag{7}$$

the curl of which is easily seen to give the positive sense to the B field rotation.

Although the vector potentials $\boldsymbol{A}$ are given in curvilinear coordinates, we evaluate them on a rectangular grid, and, for the purposes of computation, differentiate numerically. This is particularly simple in cylindrical coordinates, where $\boldsymbol{A}$ points always along the cylinder (i.e., the z) axis, and the components of its curl (i.e., of the B_1 field) lie always in the transverse plane. In the more complicated case of the sphere, the vector potential points along $\boldsymbol{\phi}$ (or ϕ'), which is chosen to circulate about the polarization axis of the corresponding $\mathbf{B}_1$. Fig. 1 illustrates the geometry, that of a transaxial image plane (labelled 'A') passing through the center of a spherical sample, itself centered at the origin of spherical coordinates. An orthogonal diametral plane, labelled B, is also inscribed in the sphere; its perimeter is an exemplary circulation path of the vector $\boldsymbol{\phi}$ as shown by the arrow head. The key point, explained in detail in the figure legend, is that $\boldsymbol{\phi}$ in this model, crosses the image plane always at normal incidence. The mathematical consequence is that all components of the curl of $\boldsymbol{A}$ (i.e., the B_1 field) will lie flat in the image plane. This simplifies the numerical coding, and insures that there can be no objection, formally, to writing all fields as a pair of rectangular components of the curl. For a *complex* vector potential $\boldsymbol{A}$, this actually results in *four* components of $\mathbf{B}_1$ inside cylinder or sphere, corresponding to directions x and y, and (per Eq. (11) below) to phase shifts of 0 and $\pi/2$:

$$\begin{aligned}B_{11} &= \mathbf{curl}_x[\boldsymbol{A}^{(1,\text{Re})} - \boldsymbol{A}^{(2,\text{Im})}], \\ B_{12} &= \mathbf{curl}_x[\boldsymbol{A}^{(1,\text{Im})} + \boldsymbol{A}^{(2,\text{Re})}],\end{aligned} \tag{8}$$

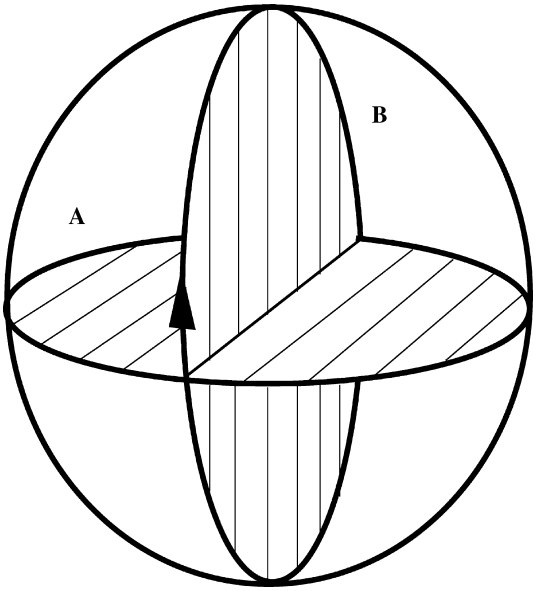

Fig. 1. Geometry for calculation of vector potential in the sphere. The plane labelled A is the diametral transaxial (or image) plane, inscribed in the sphere; the plane B is one member of an infinite family, whose members are generated by simply displacing plane B forward or backward along the direction of its normal. These planes intersect the surface of the sphere in a family of circles; and from each of the circles we may generate a further infinite family of circles by considering all circles parallel and coaxial, and lying inside the sphere. These circles define the locus of the unit ϕ vector in spherical coordinates; and each of them intersects the plane A at normal incidence, as claimed in the text; but this holds only for A a diametral plane.

$$\begin{aligned}B_{21} &= \mathbf{curl}_y[\boldsymbol{A}^{(1,\text{Re})} - \boldsymbol{A}^{(2,\text{Im})}], \\ B_{22} &= \mathbf{curl}_y[\boldsymbol{A}^{(1,\text{Im})} + \boldsymbol{A}^{(2,\text{Re})}].\end{aligned} \tag{9}$$

Note that the B fields are spatially inhomogeneous, due to the complex nature of the vector potential; and that a source, linearly polarized at infinity in free space, can produce, at different points within the dielectric sample, orthogonally directed B fields (*ergo* the indices 1 and 2, rather than x and y). It is also true in general for quadrature excitation, that the fields will exhibit (at certain points in space) elliptic polarization; but it is the circularly polarized component that is required for image calculations [12], and so must be projected out. This is expediently done for quadrature excitation by writing the usual NMR radiofrequency Hamiltonian and transforming to the rotating frame [22]. Beginning with H_{rf} in units of the reduced Planck constant:

$$H_{\text{rf}} = \omega\hbar[I_x B_x + I_y B_y], \tag{10}$$

where the real, time dependent, cartesian components of $\mathbf{B}_1$ are given in matrix form as:

$$\begin{bmatrix} B_x \\ B_y \end{bmatrix} = \begin{bmatrix} B_{11} & B_{12} \\ B_{21} & B_{22} \end{bmatrix} \begin{bmatrix} \cos\omega t \\ -\sin\omega t \end{bmatrix} \tag{11}$$

we next re-express all spin operators in the spherical tensor basis (e.g., $I_x = I_+ + I_-$), and all trigonometric

factors as sums of complex exponentials. Then, transforming the spin operators according to:

$$I_{\pm}(t) = \exp \pm \mathrm{i}\omega t I_{\pm} \tag{12}$$

and retaining only terms at zero frequency, one arrives (after reverting to cartesian components for the operators) at the transformed radiofrequency Hamiltonian in the rotating frame:

$$H_{\mathrm{rf}}^{\mathrm{T}} = \omega\hbar[I_x(B_{11} - B_{22}) + I_y(B_{12} + B_{21})], \tag{13}$$

where the spin operators are now expressed in the rotating basis, and their coefficients are the corresponding circular components of the rotating field. These field components are of course all real, given the requirement for a real Hamiltonian in whatever frame of reference. Other methods of obtaining field components stationary in time, such as simple removal of the time factor $\exp i\omega t$, or projection with the unit spherical basis vector $(1/\sqrt{2})\{\mathbf{e}_x + i\mathbf{e}_y\}$ would allow for the possibility of complex fields—useful in themselves, but inappropriate to the rotating frame in magnetic resonance. Abragam gives a clear discussion of rotating coordinates and transformations, although without the complications of a lossy dielectric medium [23].

For a small angle Gradient Recalled Echo experiment, the image intensity I is proportional to the squared magnitude of the B_1 field in the rotating frame; and we have simply:

$$I \sim |B_{11} - B_{22}|^2 + |B_{12} + B_{21}|^2, \tag{14}$$

where I is the image intensity, the tilde indicates the relationship of proportionality, and the square brackets indicate the magnitude of the quantity within. As noted above, the field components in Eq. (13) are calculated directly by numerical differentiation of the vector potentials, a multiplier is subsequently applied to scale the image for display.

The model of the cylindrical dielectric is capable of elaboration, and the excitation by an external field deus ex machina can be replaced by a two-dimensional shielded resonator (e.g., of bird cage type). This is realistic for a resonator of sufficient length, where end effects may be ignored—a condition found to be justified a posteriori, in the agreement we shall present between simulation and experiment. Then the boundary value problem for the empty antenna (i.e., absent the dielectric load) is that of one or more axial conductors inside a conductive cylinder, yielding solutions of TEM character; that is whose wave potentials satisfy a two-dimensional Laplace equation. Similar models have found successful application in the study of the mode structures of cylindrical resonators [24–26]. For a highly multipedous bird cage (say of 16 legs or more) the calculated images and flux profiles are virtually indistinguishable from those given by our simpler model, despite the presence of higher order bessel functions (cf. Appendix A), whose contribution (if it appears at all) is seen only at the periphery of the image.

This enclosed cylinder model also affords a straightforward calculation of the Q or quality factor of the conductively damped dielectric cylinder, considered itself as a resonator. We follow Collin's definition [27] of the total Q

$$Q = \frac{\omega_0(W_1 + W_2)}{(P_1 + P_2)}, \tag{15}$$

where W_1 and W_2 are the stored energies (averaged over a resonant cycle) inside and outside the dielectric, P_1 and P_2 are the dissipated power inside and the radiative loss, and ω_0 is the resonant frequency. The average internal and external electrical energies are given by the appropriate spatial integrals of the squared modulus of the electric field $\mathbf{E}$, as $(\varepsilon\varepsilon_0/4)\int |\mathbf{E}|^2 \,\mathrm{d}V$, where ε is the relative dielectric constant. The Maxwell equations for an undamped, undriven resonator have propagating solutions only at eigenfrequencies; and it may be shown [28] when the field is confined to a conductive enclosure (as is the case here) that the electric and magnetic stored energies are equal. Note that this applies to the sum of energies in Eq. (15) above, not to the internal and external components individually. Since the sum of electric and magnetic energy of the undamped resonator is conserved, it must therefore be equal to twice the electric energy discussed above. Given the character of the fields, and the large disparity in relative dielectric constants inside and outside the cylinder—a factor of 80 in the present case—it can be shown, by direct integration of the fields, that great bulk of the electric energy—over 99%—is stored inside. The problem of setting integration limits for the external energy noted by Richtmeyer [29], does not occur here, due to the presence of the shield. The rms dissipated power in the dielectric is $(\sigma/2)\int |\mathbf{E}|^2 \,\mathrm{d}V$, where σ is the conductivity, and the integration is over the interior of the dielectric. It is shown in Appendix A that the radiative dissipation due to induced shield currents is negligible in comparison to this in all cases of interest to us; therefore the total Q reduces to the simple expression $\omega_0\varepsilon\varepsilon_0/\sigma$.

Since the reasoning given above depends upon equality of stored electric and magnetic energies, which is easily justified only for the undamped resonator, we have studied the energy distribution numerically, and find (within the accuracy of our computations) that the equality holds, within 2–3%, for the conductively damped resonator, to Q values of about 10, where the resonances are still fairly well separated. Equality breaks down at very strong damping ($Q \leqslant 3$) when the overlap of neighboring resonances becomes significant, and the calculation for an uncontaminated mode is no longer (in any obvious way) possible. Given our success in using Q as a figure of merit, we believe that this breakdown is

due solely to the overlap of neighboring modes, and not to a re-distribution of energy within a particular mode.

We shall also require the Q factor for a dielectric sphere in free space. The application of a shield by analytical means poses difficulties over and above those which occur in cylindrical geometry. The situation is also complicated by the existence of different choices for the scattered potentials and the boundary conditions, which offer an array of trade-offs among simplicity, ease of calculation, and rigor. We consider three cases: (i) the resonant sphere in free space emitting a quasi-static (non-radiative) field, (ii) the resonant sphere radiating into free space, and (iii) the sphere inside a spherical conductive shell. All three are characterized by their secular equations, which we give in Appendix A. The potentials for the non-radiating sphere (our first case), here written per tesla, are $a\sin\theta\psi_1(kr)$ inside the sphere and $a^3\sin\theta r^{-2}$ outside. For a radius a of 8 cm the resonant frequency is ~208 MHz, corresponding to a free space wavelength of ~70 cm. While the integral of the scattered electric flux does not vanish at infinity, a comparison of the energy integrals inside and outside the sphere shows ~2.5% of the energy to be stored outside; a conductive surface placed at infinity has therefore but small effect on energy balance, while allowing us to good approximation to to invoke equality of electric and magnetic stored energies inside the sphere. In fact we will ignore the energy outside. Furthermore, the Q factor calculated for the radiating sphere (case (ii) above, also cf. Appendix A) is 110—an insignificant loss in comparison to that due to the large conductivities we shall deal with. In consideration of these factors for the *lossless* dielectric sphere, we conclude that the Q of the *lossy* sphere [per Eq. (15)] may be written, to at least 5% accuracy, as $\omega_0\varepsilon\varepsilon_0/\sigma$ regardless of the radiative or non-radiative nature of the external (or scattered) field.

The shielded sphere is also of practical interest, since an RF shield of some sort is always present about the sample in a high-field clinical MR scanner. The equality of stored electric and magnetic energies automatically applies here. For a shield radius corresponding to that of a typical head resonator (15–18 cm) the secular equation may be solved numerically to show that the perturbation of the resonant frequency is about 5%. We therefore conclude that the majority of electric energy is still stored the dielectric, and that our above-given expression for Q still holds.

Another significant point emerging from these discussions concerns the choice of scattered field for the sphere irradiated by a uniform magnetic field. As noted in Section 4 below, the electromagnetic field produced at the sample by a typical imaging resonator has, in fact, essentially quasi-static, and (to large degree) pure magnetic character, even at high frequencies. This justifies the choice of the exciting fields in Eqs. (2)–(5). Matching of the boundary condition in this case requires also a quasistatic field. We will use this requirement below in the calculation of flux plots for the sphere under excitation.

Finally we shall employ the vector potential for a sphere irradiated by a surface coil, which has also been treated elsewhere in the NMR literature [19,20], and which is derived in its present form (by means similar to those described for Eqs. (4) and (5)) from a formula due to Smythe [21]:

$$\boldsymbol{A} = \boldsymbol{\phi}\frac{\mu_0 I\sin\alpha}{2}\sum_{n=1}^{\infty}(a/c)^n(2n+1) \times \frac{P_n^1(\cos\alpha)P_n^1(\cos\vartheta)\psi_n(kr)}{n(n+1)ka\psi_{n-1}(ka)}. \tag{16}$$

Here α is the angle subtended from the center of the sphere to the periphery of the surface coil, c is the length of the chord defining α, the Ps are associated legendre polynomials, and other symbols have their earlier meanings. The inducing field of the surface coil is treated quasi-statically, while the full wave Maxwell equations are solved inside the sphere.

3. Results

Figs. 2A and B show the observed gradient echo image, in the transaxial plane, together with its profile, recorded at 128 MHz (B_0 of 3.0 T) for a cylindrical jug of radius 9.25 cm, filled with 0.05 M aqueous sodium chloride. Figs. 2C and D give the corresponding results for the theoretically calculated image, using the electrical parameters with $\varepsilon = 80$, and $\sigma = 0.5$ siemens/M. Note that the overall appearance of the experimental

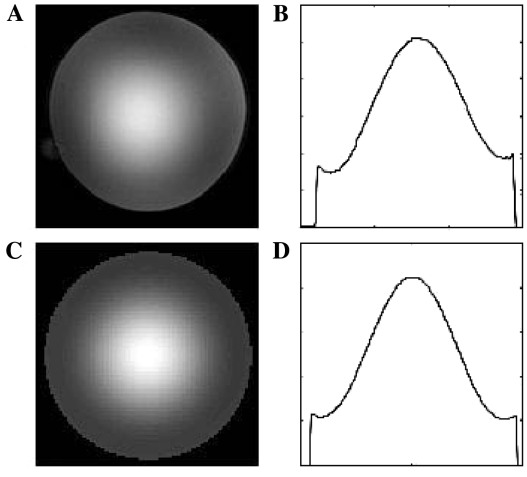

Fig. 2. Above, experimental gradient recalled proton image (20° flip angle) at 3.0 T, (A) and profile, (B) of cylindrical phantom, radius 9.25 cm, filled with 0.05 aqueous NaCl; below (C) and (D), computer simulations of same, at 128 MHz, with $\varepsilon = 80$ and $\sigma = 0.5$.

image is well reproduced by the theory, particularly the up-tick in intensity at the periphery. The failure to obtain more perfect quantitative agreement between simulated and experimental intensity ratios (peak/wings) is ascribed to partial saturation of the magnetization at the center of the phantom, due to the increased RF field strength there (vide infra). While the images here were taken with a lumped element TEM resonator (which is a low pass structure), comparable results are obtained with a high-pass bird cage resonator; in fact, we are unable to distinguish the results of different volume resonators based solely upon the brightening artifact. The brightening was clearly apparent when the phantom was imaged with a third resonator, a TEM having distributed capacitance at multiple sites along each element. Similar results for the same phantom, imaged now at 4.0 T, are given in Fig. 3. Note particularly that the theoretical images reproduce the increase (relative to 3.0 T) in the uptick of intensity, at the periphery of the phantom. The asymmetry observed at 4.0 T is ascribed to uneven reactive loading on opposite sides of the coil, rather than uneven coupling at the drive ports. Preliminary calculations and experiments have been given to support this explanation [30].

Some insight into the origin of the brightening is gained from Fig. 4, which depicts snapshots in a time sequence of the rotating RF flux contours in the laboratory frame—calculated directly from the iso-contours of Eq. (6), and given for the positive sense of rotation. The plots exhibit a characteristic screw propellor form

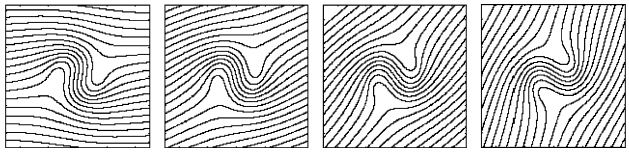

Fig. 4. Time exposures of CCW rotating flux plot for quadrature excitation of lossy dielectric cylinder, at 128 MHz, with $\varepsilon = 80$ and $\sigma = 0.5$. The contours are calculated from Eq. [6] at various values of the time. Since the vector potential points out of the viewing plane, its iso-contours are in fact the flux lines traditionally used to represent the magnetic field.

[22], with the flux lines bunched at the center of the cylinder and dispersed towards its periphery. The regions of high flux (and high field) correspond, obviously, to higher intensity of the image, with the effect being averaged over the rotation of the contours.

It is instructive to perform similar calculations of flux plots and images for a spherical phantom, using the vector potentials of Eqs. (4) and (5), particularly near a resonant condition of the sphere (of 8 cm radius), as we pass through the condition (well known in the theory of oscillation) of critical damping, i.e., Q factor $= 0.5$. Fig. 5 gives a pair of time-course snapshots, at 208 MHz, for each of two conditions: underdamped, $Q = 0.9$ ($\varepsilon = 80$, $\sigma = 1$) and overdamped, $Q = 0.3$ ($\varepsilon = 80$, $\sigma = 3$). The difference is marked. Flux is drawn in and concentrated at the center of the underdamped sphere; flux is expelled from the center of the overdamped sphere, and concentrated at the periphery.

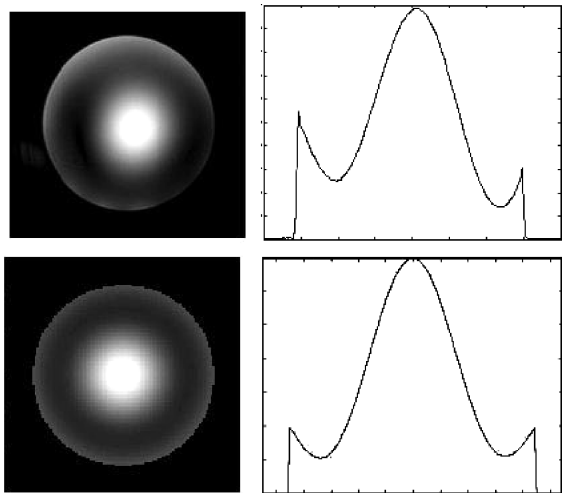

Fig. 3. As in Fig. 2 above, except images taken at 4.0 T, and simulations done at 170 MHz. The asymmetry of the experimental image and profile is due apparently to distortion of the RF homogeneity, probably due to reactive loading of resonator by the phantom, as noted in the text. For reference, the radiofrequency polarization planes (defined by the drive ports of the coil) are parallel to the (vertical and horizontal) figure axes. Inasmuch as the phantom is roughly (but imperfectly) centered in the coil, the drive axes intersect at a point slightly above (we estimate 2–3 cm) its center. The two drive ports are located above and to the viewer's left.

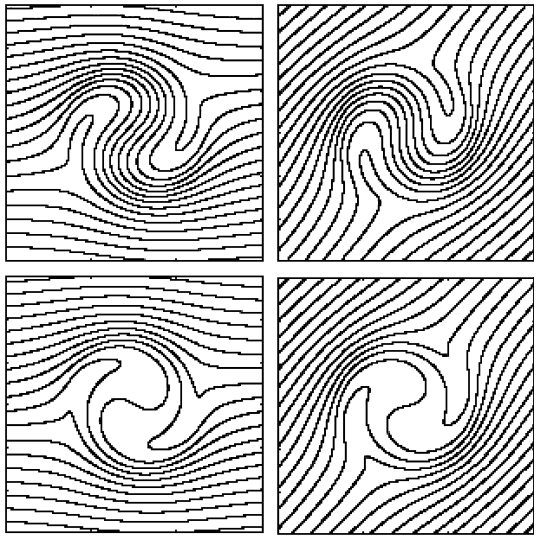

Fig. 5. Time exposures of CCW rotating flux for quadrature excitation at 208 MHz of a lossy dielectric sphere, of radius 8 cm, viewed in a diametral plane, for two conditions of damping: (i) above, left and right, sphere underdamped, $Q = 0.9$ ($\varepsilon = 80$, $\sigma = 1$); and (ii) below, left and right, sphere overdamped, $Q = 0.3$ ($\varepsilon = 80$, $\sigma = 3$). Referring to Fig. 1, the vector potential in the diametral plane points perpendicular to that plane (the viewing plane) so that the iso-contours of vector potential are true flux lines, as explained in the legend to Fig. 4.

Similar effects are shown in Fig. 6 for the model of the dielectric cylinder enclosed in a shielded resonator, introduced above. The dimensions of the cylinder and resonator are chosen to match our experimental conditions. The frequency—157 MHz—is the resonant frequency of the dielectric inside the resonator (cf. Appendix A), and the conductivities—0.7 (above) and 2.0 (below)—correspond to Q values of 1.0 and 0.35. The behavior of the flux contours upon passage through critical damping ($Q = 0.5$) is comparable to that observed for the sphere in Fig. 5.

The passage through critical damping also appears in plots of the resonant denominators versus frequency, at different conductivities corresponding to under-damped and over-damped conditions. This is shown in Fig. 7, where we plot the inverse magnitude of $\psi_0(ka)$ [cf. Eqs. (4) and (5)] from 1 to 500 MHz, at four values of the conductivity σ. For the σs of 0.3, 0.5, and 0.8 siemens/M, distinct peaks resembling resonant responses (and sharper at smaller σ) are seen at about 210 and 420 MHz. The behavior for $\sigma = 2$ siemens/M (overdamped in this frequency range) is qualitatively different, exhibiting no resonant like responses, but only a steady decrease from the frequency origin. Instructive examples of this type of calculation have also been given elsewhere [8].

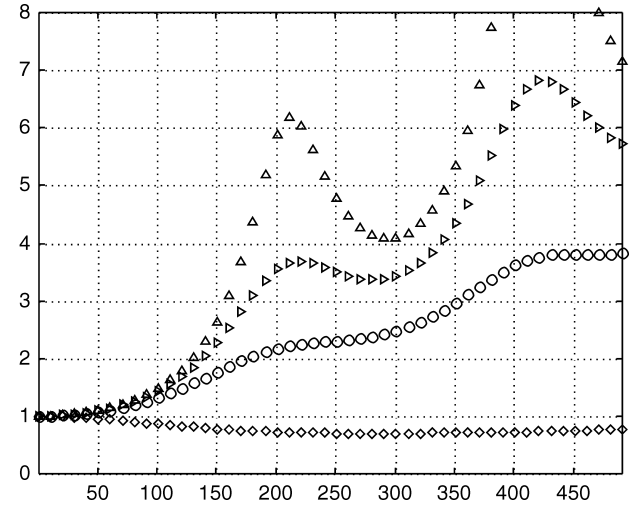

Fig. 7. Plots of the inverse resonant denominator, $1/|\psi_0(ka)|$, for the sphere of dielectric constant $\varepsilon = 80$, at various values of the conductivity: $\sigma = 0.3$ (vertical triangles), $\sigma = 0.5$ (sloping triangles), $\sigma = 0.8$ (circles), $\sigma = 2$ (diamonds). The first three values of σ represent an underdamped condition for the resonances in question; the last an overdamped condition. Refer to the text for further discussion.

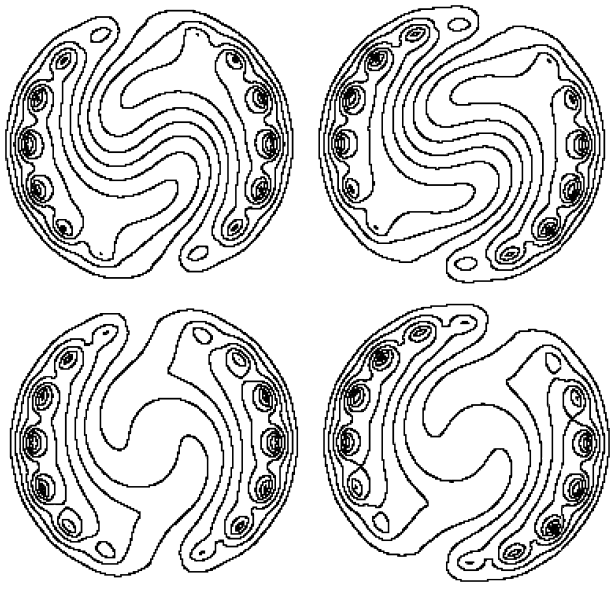

Fig. 6. Similar to Fig. 5, but for dielectric cylinder inside a shielded cylindrical resonator, and at two conditions of damping. Time exposures of CW rotating flux for quadrature excitation at 157 MHz of a lossy dielectric cylinder, of radius 9.25 cm, viewed in a diametral plane, for two conditions of damping: (i) above, left and right, underdamped, $Q = 1.0$ ($\varepsilon = 80$, $\sigma = 0.7$); and (ii) below, left and right, overdamped, $Q = 0.35$ ($\varepsilon = 80$, $\sigma = 2$). The cylindrical resonator is assumed to be bird cage type with 16 elements on a bolt circle of radius 14.6 cm, and a cylindrical shield of radius 17.7 cm. (This matches the dimensions of our experimental resonator.) The current distribution is assumed to be sinusoidal. As in earlier figures of this type, the vector potential points perpendicular to viewing plane so that the iso-contours of vector potential are true flux lines, again, as explained in the legend to Fig. 4.

Resonant effects are also expected for a sphere irradiated by a surface coil. Examination of Eq. (16) (and comparison with Eq. (4)) shows that the vector potential

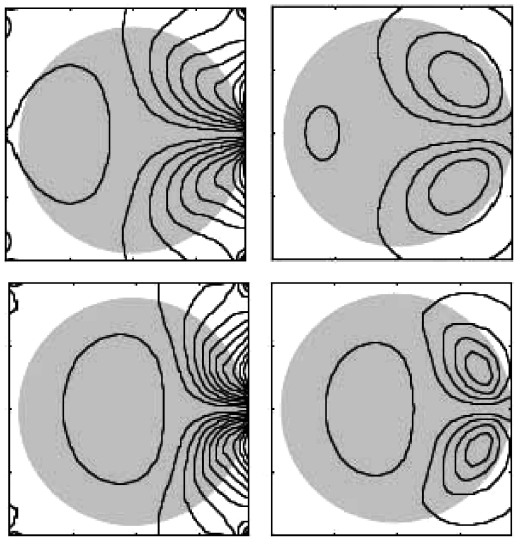

Fig. 8. Time exposures of flux contours for excitation of a lossy dielectric sphere of radius 8 cm by a surface coil, at 208 MHz. The arrangement is similar to Fig. 5 as regards viewing plane and electrical parameters. The surface coil is a circular loop of radius 2 cm, lying just to the right of the sphere with its plane perpendicular to the paper. While the coil itself out of sight, its flux lines are clearly seen, emanating from the right of each sub-figure. The distance from the center of the sphere to any point on the periphery of the coil is 12 cm. The two conditions of damping are: (i) above, left and right, sphere underdamped, $Q = 0.9$ ($\varepsilon = 80$, $\sigma = 1$); and (ii) below, left and right, sphere overdamped, $Q = 0.3$ ($\varepsilon = 80$, $\sigma = 3$). The view is of a diametral plane; the flux contours therefore represent true field lines (cf. legends to Figs. 4 and 5 above).

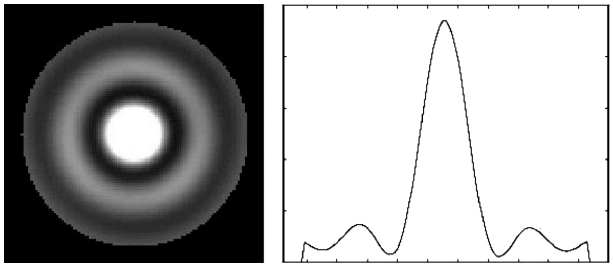

Fig. 9. Comparison with results of [8]. Calculated small tip, gradient recalled, transaxial image with volume quadrature excitation and reception, at 400 MHz, for a dielectric sphere, radius 10 cm, ($\varepsilon = 80$, $\sigma = 0.5$).

in this case is a weighted sum of terms, each containing the (potentially) resonant factor

$$f_n = \frac{P_n^1(\cos\vartheta)\psi_n(kr)}{\psi_{n-1}(ka)}. \tag{17}$$

In the vicinity of 200 MHz, only the $n = 1$ term shows resonant behavior, but on this basis alone, it produces noticeable effects upon passing through critical damping. This is seen in Fig. 8, which repeats the calculations of Fig. 5, but with irradiation by a surface coil rather than by a uniform radiofrequency B field. Two points emerge: the first is that at high, but still sub-critical damping, flux is drawn in towards the center of the sphere, while in comparison, at overdamping, flux is visibly expelled from the center. The second is that even under highly damped conditions, flux penetrates (albeit weakly) all the way through the sphere.

Finally, since our method of solution for the vector potential in the sphere differs considerably from that in the recent magisterial treatment by Hoult [8], it is worthwhile to demonstrate the equivalence of the two approaches, by repeating a calculation of his, for a sphere of 10 cm radius, at 400 MHz, with $\varepsilon = 80$ and $\sigma = 0.5$. Our Fig. 9 gives the image and profile, which will be seen to reproduce virtually exactly the corresponding result of [8, Fig. 4].

4. Discussion

As magnetic resonance imaging pushes towards higher static fields and frequencies, the importance of electromagnetic wave phenomena in vivo has forced itself upon our attention, and has attracted a large community of investigators. These divide into two opposing yet complementary camps: those who solve the Maxwell equations by purely numerical means, and those who favor (at least partially) an analytic approach. Among the analysts, some of the pioneers of the subject have treated the cylindrical resonator with wave-guide models, which emphasize the importance of the axial propagation constant and the interaction of the resonator with the sample to be imaged [4,5,7]. Others (whom the present writer has followed) have opted for simpler models in which axial propagation does not figure, and where the resonator is either ignored [12], or does plays at most a minor role. Our success in performing accurate image simulations, with what amounts to a two-dimensional calculation, leads us to devalue any specific rôle for electromagnetic propagation or retardation effects in the irradiating resonator per se, in the formation of the brightening artifact. For example, the current in a high Q coaxial resonator, even one which spans several wavelengths, has only two phases: 0 and π, which is to say, that at resonance, all metal antennas behave similarly, regardless of electrical length.

The simplicity of our analytical model, particularly the use of a quasi-static field outside the phantom, may also be justified on a priori grounds, For a long shielded bird cage, or TEM resonator, the electromagnetic potentials in the empty resonator, well away from the periphery, must satisfy a two-dimensional Laplace equation; that is to say, they must be indistinguishable from quasistatic (or, for that matter, static) potentials. Similar reasoning may well apply to unshielded resonators in solenoidal imaging magnets, fitted (as most nowadays are) with an RF shield to isolate the gradient set. Furthermore, it is well known on circuit theoretic grounds that cylindrical resonators (of the bird cage or TEM type) possess a virtual ground plane, perpendicular to the cylinder axis, and halfway along its length (the meridian plane). All irrotational electric fields must vanish in this plane; leaving (in our model) only the solenoidal Faraday's law field. That this field in itself carries an insignificant portion of the net circuit energy is shown by the success of (suitably parametrized) circuit models in predicting the mode positions of cylindrical resonators, even to frequencies approaching 400 MHz [24]. It is worthwhile remembering in this context that electric and magnetic energy storage, in a resonator, are, unlike that in free space, spatially localized. It is probably fair to say that most electric energy storage in typical NMR resonators (even for large resonators at high fields) is localized around the capacitance, even if that is distributed rather than lumped. This also suggests the inapplicability to NMR problems of scattering models in which the incident field is free space TEM, i.e., having equal storage of electric and magnetic energy at any point in space.

Our results also point strongly to the idea that center brightening is a direct result of dielectric resonance; but given the general complexity of conditions, that term will require some qualification. Inasmuch as resonance occurs generically within objects capable of supporting wave phenomena, and having reflective boundaries, it is more or less self evident that a sphere or cylinder of dielectric constant 80 should support a resonance—given that the impedance mismatch with free space is on the order of 9, leading to a reflection coefficient on the order

of 0.8. Two competing effects are at work: here: the high dielectric constant tends to focus the flux in the center of the irradiated object, while increasing conductivity tends to the push the flux towards the periphery—essentially a skin effect. The relative importance of each of these tendencies is measured by the Q or quality factor of the dielectric object. The field focussing effect predominates at sufficiently high Q, and the skin effect at sufficiently low; the crossover point between 'sufficiently high' and 'sufficiently low' is that of critical damping, i.e., $Q = 0.5$. The fact that flux focusing is observed at frequencies far removed from the center of the dielectric resonance appears to us essentially as an instance of a resonator driven, so to speak, in the wings of its response. This is particularly so for the low (but still underdamped) Q factors of $\sim$1, occurring in many cases of interest. The sphere excited by a uniform field shows these effects very clearly; the sphere excited by a surface coil less so. This is in consequence of the sum of terms which describe the surface coil. Still, in the case of high Q, on resonance, the resonant denominator of the first term can be made to dominate, leading to a result not much distinguished from that of excitation with a uniform field.

We may elaborate these points. In the simplest instance, the uniform B field excites the pure TE_{110} mode of the dielectric sphere; and at high Q, where the imaginary component of the vector potential contributes little, the field intensity undergoes a cycle of growth and decay, while the field direction is unchanged. That is to say, the time course resembles that of a standing wave on a string, which can be written as the product of a spatial function and a time varying sinusoid. As damping increases however, the imaginary contribution grows, and the field now varies in both intensity and direction, over the period of resonance. Mathematically, the flux assumes the form of our Eq. (6) (vide supra) and can no longer be even approximately factored into a space and a time varying component. Qualitatively then, the moderately damped sphere requires a somewhat expanded notion of what, in the simplest instance, is meant by resonance; but quantitatively, the case may be unambiguously judged by the demarcation point of critical damping.

The sphere driven by a surface coil presents a more complex case, in which simultaneous excitation of a series of modes yields a sort of wave packet, which propagates across the sphere periodically at the drive frequency. The exact character of the packet is determined by the values of the individual mode functions at the drive frequency. If that mode is underdamped whose resonant frequency falls nearest that of the drive, we may say that dielectric resonance obtains, and predict that flux will be drawn towards the center of the sphere. This can occur even as the excitation wavefront appears to propagate across the sphere. Nonetheless, we must emphasize that our explicit treatment has been restricted to drive applied in the vicinity of low order modes of the sphere, e.g., $n = 1, 2$, in Eq. (17). The situation for excitation of very high order modes (e.g., $n > 10$) may soon arrive at the point where interpretation is difficult, though we believe that the Q factor would still be a useful guide.

Finally it is worth noting, that despite our frequent usage of complex variables, all actual RF potentials and fields are reduced to real quantities. This avoids the appearance of imaginary cartesian field components in the rotating frame, which, as noted, would lead to a complex and therefore non-physical Hamiltonian. This does not of course preclude the writing of the Hamiltonian as a contraction of spherical tensors, in which individual complex elements are always summed with their conjugates, leading in the end to a purely real result. See again Abragam's expression for the interaction energy of a spin with a circularly polarized radiofrequency B field [23].

5. Experimental section

All images were acquired on General Electric scanners, at static fields of 3.0 or 4.0 T, using gradient recalled echoes with spoiling, at a tip angle of 20°; the echo and repetition times were 6.5 ms (TE) and 500 to 1000 ms (TR). The phantom solutions were reagent grade NaCl in tap water. All TEM resonators employed discrete element (as opposed to transmission line) components, as described elsewhere [31]; further details of construction and geometry have also been given [32,33]. The TEM resonators for 3.0 T were end capped i.e., bucket shaped, as was the 3.0 T bird cage resonator; the 4.0 TEM resonator was cylindrical with no end cap. The bird cage circuit was of high-pass type.

All electromagnetic and image simulations were done using scripts written for the purpose at hand in Matlab 5.2 for Macintosh (Mathworks). Our method of image simulation was developed and validated for cylindrical resonators having quadrature excitation and reception, and is not advertised for use in other contexts.

Acknowledgments

This work was supported by General Electric Medical Systems. The author thanks Mr. Paul Calderon for his indispensable help in designing mechanical parts and circuit boards for the resonators, and Mr. Jerry Dahlke for assisting with the experiments at 4.0 T.

Appendix A

We here describe our solution of the two-dimensional boundary value problem for a shielded cylindrical resonator (e.g., of bird cage type), loaded coaxially with a lossy dielectric cylinder. Our result is similar to that gi-

ven in a useful report by Spence and Wright [34], which appeared during the review cycle of the present work, although our assumptions and methodology differ from theirs at certain key points.

We have given above, in the body of the main text, the rationale and evidence for assuming the field in the empty shielded resonator to be of TEM character. Briefly, the presence of axial conductors enforces the TEM condition. The axial and transverse field boundary value problems are then perfectly separated, and the axial propagation constant (if it appears at all) is absent from the argument of the radial wave function. This is in contrast to the case of a perfectly hollow waveguide, which demands TE or TM boundary conditions, for which the axial and transverse problems are not decoupled, and the axial propagation constant is calculated in relation to the cutoff frequency, and appears explicitly in the argument of the radial wave function.

With the introduction of the dielectric load, we must consider separately the filled and unfilled regions inside the shield. We assume that the two-dimensional Laplace equation continues to hold good in the unfilled region; while in the filled region a two-dimensional Helmholtz equation is needed, to account for the electrical properties of the load, as embodied in a radial wave vector. According to the usual theory for dielectrically loaded waveguides, axial propagation (inasmuch as it enters our particular problem at all) must be the same in both the filled and empty regions [35].

We first solve the primordial boundary value problem of a single line current irradiating the load. The solution for the entire resonator is then built up by azimuthally displacing the primordial solution, weighting according to known (sinusoidal) current distribution, and adding.

The vector potential of the line current is given by a two-dimensional Green's function; the shield is modelled by an opposed image current [36]. In the fully realized solution, the primary and shield currents reside on a pair of bolt circles, of radii designated r_{01} and r_{02}, whose geometric mean r_s is the shield radius. A scattered potential is then constructed whose form automatically satisfies the boundary condition at the shield, regardless of any weighting coefficient. The induced potential inside the dielectric is determined by need for a non-singular solution of the two-dimensional Helmholtz equation. The excitation, induced, and scattered potentials all meet at the cylinder radius, where they must satisfy the twin boundary conditions of continuity, and continuity of the azimuthal magnetic field. The mathematical details are as follows.

The vector potential for excitation by a pair of opposed line currents, at radii r_{01} and r_{02} (vide supra) is:

$$\boldsymbol{A}^{\text{source}} = \frac{\mathbf{e}_z \mu_0}{2\pi}\left[\sum_{n=1}^{\infty}\frac{1}{n}\left\{\left(\frac{r}{r_{01}}\right)^n - \left(\frac{r}{r_{02}}\right)^n\right\}\cos n\vartheta + \ln r_{02} - \ln r_{01}\right], \quad a < r < r_{01}, \tag{A.1}$$

$$\boldsymbol{A}^{\text{source}} = \frac{\mathbf{e}_z \mu_0}{2\pi}\left[\sum_{n=1}^{\infty}\frac{1}{n}\left\{\left(\frac{r_{01}}{r}\right)^n - \left(\frac{r}{r_{02}}\right)^n\right\}\cos n\vartheta + \ln r_{02} - \ln r\right], \quad r_{01} < r < r_s, \tag{A.2}$$

where a is the cylinder radius, μ_0 us the free space permeability, and other symbols have been defined in the main text. The induced potential (inside the cylinder) and the scattered (outside) are

$$\boldsymbol{A}^{\text{cyl}} = \frac{\mathbf{e}_z \mu_0}{2\pi}\left[\sum_{n=1}^{\infty} B_n J_n(kr)\cos n\vartheta + B_0 J_0(kr)\right], \quad r < a, \tag{A.3}$$

$$\boldsymbol{A}^{\text{scat}} = \frac{\mathbf{e}_z \mu_0}{2\pi}\left[\sum_{n=1}^{\infty} A_n\left\{\left(\frac{r_s}{r}\right)^n - \left(\frac{r}{r_s}\right)^n\right\}\cos n\vartheta + A_0 \ln r\right], \quad a < r < r_s, \tag{A.4}$$

where A_n and B_n are given by

$$A_n = \frac{\left\{\left(\frac{1}{r_{02}}\right)^n - \left(\frac{1}{r_{01}}\right)^n\right\} + B_n J_n(ka)}{\left\{\left(\frac{r_s}{a}\right)^n - \left(\frac{a}{r_s}\right)^n\right\}}, \tag{A.5}$$

$$\begin{aligned} B_n = {} & \left(\left\{\left(\frac{a^{n-1}}{r_s^n}\right)^n + \left(\frac{r_s^n}{a^{n+1}}\right)^n\right\}\left\{\left(\frac{a}{r_{01}}\right)^n - \left(\frac{a}{r_{02}}\right)^n\right\}\right. \\ & \left. - a^{n+1}\left\{\left(\frac{1}{r_{01}}\right)^n - \left(\frac{1}{r_{02}}\right)^n\right\}\left\{\left(\frac{r_s}{a}\right)^n - \left(\frac{a}{r_s}\right)^n\right\}\right) \Big/ \\ & \left(n\left\{\left(\frac{a^{n-1}}{r_s^n}\right)^n + \left(\frac{r_s^n}{a^{n+1}}\right)^n\right\} J_n(ka) \right. \\ & \left. - \left\{\left(\frac{r_s}{a}\right)^n - \left(\frac{a}{r_s}\right)^n\right\} k J_n'(ka)\right), \end{aligned} \tag{A.6}$$

$$A_0 = B_0 k a J_0'(ka), \tag{A.7}$$

$$B_0 = \frac{\ln r_{02} - \ln r_{01}}{J_0(ka) - ka J_0'(ka)\ln a}. \tag{A.8}$$

The homogeneous equations (without the driving term) are also of interest. For the principal mode ($n = 1$) of the cylinder in free space, the vanishing of the secular determinant gives the condition $J_0(ka) = 0$, which is also the resonant condition in Eq. (2) of the main text. For a lossless cylinder with $\varepsilon = 80$ and radius 9.25 cm (as used in the text above) the resonant frequency is ~142.5 MHz. For the enclosed cylinder model, existence of a solution to the homogeneous equations requires the condition

$$\det\begin{bmatrix} -\left\{\left(\frac{r_s}{a}\right)^n - \left(\frac{a}{r_s}\right)^n\right\} & J_n(ka) \\ n\left\{\left(\frac{a^{n-1}}{r_s^n}\right) - \left(\frac{r_s^n}{a^{n+1}}\right)\right\} & k J_n'(ka) \end{bmatrix} = 0 \tag{A.9}$$

be met. Using parameters which match the dimensions of the shielded bird cage employed in this study (rods on

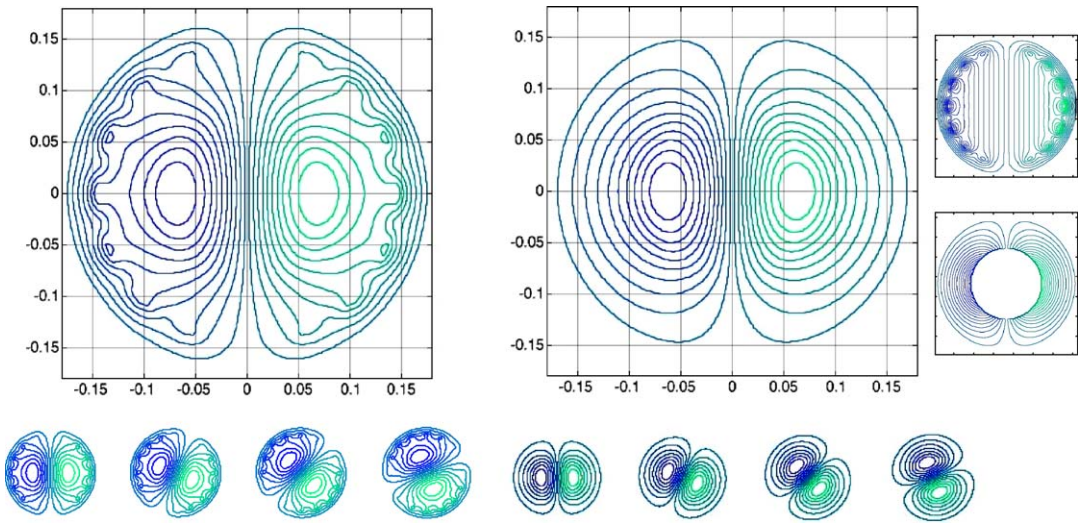

Fig. 10. Flux contours—at 142 MHz (left) and 157 MHz (right)—for the lossless dielectric cylinder ($\varepsilon = 80$) enclosed in a cylindrical resonator of bird cage type, with 16 elements. Cylinder and resonator geometries as in Fig. 6 of the main text. The two frequencies here are the resonant frequencies of the cylinder in free space (142 MHz) calculated from Eq. (2) of the main text and and the resonant frequency inside the shielded resonator, shifted upwards to 157 MHz, as calculated from Eq. (A.9). Both are contoured at an interval of 0.05 full excursion, to illustrate to relative concentration of flux in the phantom as true resonance is approached inside the shield; that is, below resonance, the current carrying rods of the resonator are clearly visible, whereas at resonance, they disappear in this contour scheme. Exemplary rotating flux plots are also shown below; and in the inset (far right) are given the flux patterns of the empty resonator (above) and of the scattered field alone (below) illustrating the matching of the boundary condition at the shield. The color scheme is used to indicate the transition from positive (green) to negative (blue) values of the vector potential.

bolt circle of radius 14.6 cm and shield radius of 17.7 cm) we calculate a resonance frequency shifted upwards from its free space value, to ~157 MHz—presumably because the shield lowers the effective inductance.

Fig. 10 shows the flux contours for the cylinder-in-resonator at both the natural free space (left) and the upwardly pulled frequencies (center-right). Both are contoured at an interval of 0.05 full excursion, to illustrate to relative concentration of flux in the phantom as true resonance is approached; that is, below resonance, the current carrying rods of the resonator are clearly visible, whereas at resonance, they disappear in this contour scheme. Exemplary rotating flux plots are also shown below; and in the inset (far right) are given the flux patterns of the empty resonator (above) and of the scattered field alone (below) illustrating the matching of the boundary condition at the shield.

Fig. 11 shows the simulated gradient-recalled image image and profile, at 128 MHz, for a dielectric cylinder—of the same size and electrical properties as that used in the calculations for Fig. 2—but now placed inside our model shielded resonator. Despite some differences in the layout, the results of Figs. 2 and 11 are seen to be highly similar, as regards intensity ratios, upticks, location of inflexion points, etc.—showing that the addition of the shield does not change the fundamentals, even despite the upward frequency shift. Doubtless, however, there could be found conditions (e.g., a low loss sample near resonance in free space) where a larger difference would be apparent.

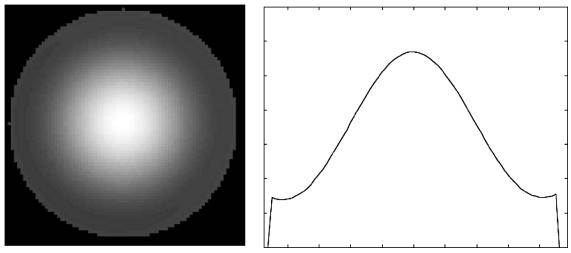

Fig. 11. Simulated gradient-recalled image image and profile, at 128 MHz, for a sample of the same size and electrical properties as that used in the calculations for Fig. 2, but inside the shielded resonator whose dimensions equal those of the shielded bird cage used in our imaging experiments (cf. Fig. 6, legend) as well as all other simulations. Despite differing layout and aspect ratio, the intensity ratios (peak to wings), as well as the qualitative features such as the location of inflexion points in profile, and peripheral uptick in intensity, are seen to be essentially the same as for Fig. 2.

The power dissipated in the walls of the RF shield, at frequency ω, per unit drive current applied, is (per meter of axial extension):

$$P(\omega) = \frac{\pi s(\omega) N}{2 r_s} \sum_n n^2 |A_n|^2. \tag{A.10}$$

where $s(\omega)$ is the frequency dependent surface resistance ($\sim 2.6 \times 10^{-7} \times \sqrt{(\omega/2\pi)}$ for copper) N is the number of resonator legs, and other symbols have been defined. (Recall that A_n is dimensionless, $s(\omega)$ has the units of resistance, and the whole expression must be multiplied by a length and the square of a unit current.) The Q

factor arising from dissipation in the shield for a driven coil (with dimensions given above) loaded with a cylinder of 0.05 M aqueous saline, at 128 MHz is about 3×10^3. Since we are chiefly concerned with Q values in the vicinity of critical damping, i.e., on the order of unity, this radiative damping is for our purposes negligible.

Some related problems of the dielectric sphere are also of interest. For the resonant sphere of radius a and wave vector k [cf. Eq. (1)], emitting a quasi-static (non-radiating) field into free space, the boundary value problem of the TE_{110} mode reduces to the secular equation:

$$\det \begin{bmatrix} \psi_1(ka) & -\frac{1}{a^2} \\ k\psi_1'(ka) & \frac{1}{a^2} \end{bmatrix} = 0, \tag{A.11}$$

which is solved analytically by $\psi_0(ka) = 0$ (satisfied for $ka = \pi$). For a radius of 8 cm, and relative dielectric constant of 80, the resonant frequency is ~208 MHz.

A modern treatment of the resonant sphere radiating into free space, is given by Collin [27]. The secular equation is for the TE_{n10}: mode is

$$\det \begin{bmatrix} \psi_n(ka) & -h_n^{(2)}(k_0a) \\ k\psi_n'(ka) & -k_0h_n'^{(2)}(k_0a) \end{bmatrix} = 0, \tag{A.12}$$

where $h_n^{(2)}(kr)$ is the spherical hankel function [37] of degree 2 and order n, k_0 is the free space wavevector, and k is the wave vector inside the sphere, which is assumed to embody zero conductivity, but which acquires a damping factor due to radiation, as appears in the solution. Collin obtains a Q of 140 (independent of radius) for $n = 1$, by an analytical approximation for the TE_{110} mode with relative dielectric constant $\varepsilon = 86$. We use a numerical search algorithm to obtain for $\varepsilon = 80$ a resonant frequency of 205 MHz and a Q of 110. In either case, radiative losses are small.

While we shall shall not attempt an elaborate treatment, the dielectric sphere inside a conductive spherical shell offers an analytical approximation to the sphere inside a bucket resonator (i.e., with cylindrical shield and end cap, and open only at the front). For a and b the radii of the sphere and shell, and k and k_0 the wave vectors in the dielectric and in free space, the resonant frequency of TE_{110} mode is given by the secular equation:

$$\det \begin{bmatrix} \psi_1(ka) & -\psi_1(k_0a) & -y_1(k_0a) \\ k\psi_1'(ka) & -k_0\psi_1'(k_0a) & -k_0y_1'(k_0a) \\ 0 & \psi_1(kb) & y_1(kb) \end{bmatrix} = 0, \tag{A.13}$$

where $y_1(kr)$ is the spherical Neumann function [37] of order 1, and other symbols have been defined. While this is a traditional loaded cavity problem, in fact, either the shield radius or the dielectric constant of the load may be made to dominate the determination of the resonant frequency, depending upon the relative values of the radii a and b. For the dielectric sphere we consider, with $a = 8$ cm, and a reasonable shield radius $b = 15$ cm, the frequency is dominated by the sphere and, has virtually the same value as the lossless dielectric sphere in free space: 208 MHz.

Appendix B. Generalized reciprocity in NMR

Insko et al. [17] have recently shown that the quasi-static free space Green's function, $1/r$, can be replaced by that for the Helmholtz equation, $\exp(ikr)/r$, without affecting the general form of the Hoult–Richards [15] reciprocity formula. However, it applies only to cases where the electrical properties of the sample are uniform throughout space, or where the resonator is actually immersed in the sample material; that is to say, it does not explicitly address the question of boundary conditions between media of differing properties, which are typical of NMR experiments. Inasmuch as one may posit the existence of a generalized Green's function which satisfies all boundary conditions, it is straightforward (virtually tautological) to cast the reciprocity formula in such terms. Specifically, for Green's function $G(\boldsymbol{r}, r')$ we express the flux ϕ as:

$$\phi = \int \mathrm{d}\mathbf{s} \int \mathbf{M}(\boldsymbol{r}') \cdot \mathbf{grad} G(\boldsymbol{r}, \boldsymbol{r}') \, \mathrm{d}^3\boldsymbol{r}', \tag{B.1}$$

where $\mathbf{M}(\boldsymbol{r}') \, \mathrm{d}^3\boldsymbol{r}'$ is the local dipole moment, the line integral is over the current path of the NMR coil, and the equation is obtained from the quasistatic result for a current loop [38], by substituting the generalized Green's function for $1/r$. Then noting that:

$$\mathbf{B} = \mathbf{curl} \int G(\boldsymbol{r}, \boldsymbol{r}') \mathbf{J}(\boldsymbol{r}') \, \mathrm{d}^3\boldsymbol{r}' \tag{B.2}$$

and that $\mathrm{d}\mathbf{s}$ and $\mathbf{J}\,\mathrm{d}\mathbf{r}$ are co-linear for filamentary currents, a rearrangement of the vector triple product immediately recovers the Hoult–Richards formula, valid under any conditions for which the nuclear magnetization does not appreciably alter the net electromagnetic free energy.

References

[1] P. Röschmann, Radiofrequency penetration and absorption in the human body: limitations to high-field whole-body nuclear magnetic resonance imaging, Med. Phys. 14 (1987) 922–931.

[2] P. Röschmann, Imaging of dielectric resonance mode patterns with a 4 T whole body MR system, in: Proceedings of the Seventh SMRM, 1988, p. 267.

[3] P. Röschmann, in: Proceedings of the ISMRM Workshop on High Field Engineering, 1999, p. 4.

[4] T.K. Foo, C.E. Hayes, Y.W. Kang, An analytical model for the design of RF resonators for MR body imaging, Magn. Reson. Med. 21 (1991) 165–177.

[5] T.K. Foo, C.E. Hayes, Y.W. Kang, Reduction of RF penetration effects in high field imaging, Magn. Reson. Med. 23 (1992) 287–301.

[6] S. Crozier, I.M. Brereton, F.O. Zelaya, W.U. Roffmann, D.M. Doddrell, Sample-induced RF penetration in high-field, high-resolution NMR spectroscopy, J. Magn. Reson. 126 (1997) 39–47.
[7] D.C. Alsop, T.J. Connick, G. Mizsei, A spiral volume coil for improved RF field homogeneity at high static magnetic field strength, Magn. Reson. Med. 40 (1998) 49–54.
[8] D.I. Hoult, Sensitivity and power deposition in a high-field imaging experiment, J. Magn. Reson. Imaging 12 (2000) 46–67.
[9] J.T. Vaughan, M. Garwood, C.M. Collins, W. Liu, L. DelaBarre, G. Adriany, P. Andersen, H. Merkle, R. Goebel, M.B. Smith, K. Ugurbil, 7 vs. 4 T: RF power, homogeneity, and signal-to-noise comparison in head images, Magn. Reson. Med. 46 (2001) 24–30.
[10] T.S. Ibrahim, R. Lee, A.M. Abduljalil, B.A. Baertlein, P.-M. Robitaille, Dielectric resonances and $B(1)$ field inhomogeneity in UHFMRI: computational analysis and experimental findings, J. Magn. Reson. Imaging 19 (2001) 19–26.
[11] Q.X. Yang, J. Wang, X. Zhang, C.M. Collins, M.B. Smith, H. Liu, X.H. Zhu, J.T. Vaughan, K. Ugurbil, W. Chen, Analysis of wave behavior in lossy dielectric samples at high field, Magn. Reson. Med. 47 (2002) 982–989.
[12] G.H. Glover, C.E. Hayes, N.J. Pelc, W.A. Edelstein, O.M. Mueller, H.R. Hart, C.J. Hardy, M. O'Donnell, W.D. Barber, Comparison of linear and circular polarization for magnetic resonance imaging, J. Magn. Reson. 64 (1985) 255–270.
[13] P.S. Tofts, Standing waves in uniform water phantoms, J. Magn. Reson. B 104 (1994) 143–147.
[14] D. Landau, L. Lifschitz, Electrodymanics of Continuous Media, Pergamon, 1960, Chapter VII.
[15] D.I. Hoult, R.E. Richards, The signal-to-noise ratio of the NMR experiment, J. Magn. Reson. 24 (1976) 71–85.
[16] D.I. Hoult, C.-N. Chen, V.J. Sank, Quadrature detection in the laboratory frame, Magn. Reson. Med. 1 (1984) 339–353.
[17] E.K. Insko, M.A. Elliott, J.C. Schotland, J.S. Leigh, Generalized reciprocity, J. Magn. Reson. 131 (1998) 111–117.
[18] A. Sommerfeld, Partial Differential Equations in Physics, Academic Press, New York, 1949, Chapter IV.
[19] J.W. Carlson, Radiofrequency propagation in conductive NMR samples, J. Magn. Reson. 78 (1988) 563–573.
[20] J.R. Keltner, J.W. Carlson, M.S. Roos, S.T.S. Wong, T.L. Wong, T.F. Budinger, Electromagnetic fields of surface coil in vivo NMR at high frequencies, Magn. Reson. Med. 22 (1991) 467–480.
[21] W.R. Smythe, Static and Dynamic Electricity, third ed., McGraw Hill, New York, 1968, Chapter X.
[22] J. Tropp, J. Dahlke, A simple two-dimensional model for dielectric resonance, in: Proceedings of the International Society of Magnetic Resonance in Medicine, 2000, p. 1408.
[23] A. Abragam, The Principles of Nuclear Magnetism, Oxford, London, 1961, p. 22 ff.
[24] J. Tropp, J.T. Vaughan, The prospects for systematic design of TEM resonators, in: Proceedings of the ISMRM, 1999, p. 421.
[25] B.A. Barthlein, O. Ozbay, T. Ibrahim, R. Lee, Y. Yu, A. Kangarlu, P.-M. Robataille, Theoretical model for an MRI radiofrequency resonator, IEEE Trans. Biomed. Eng. 47 (2000) 535–545.
[26] G. Bogdanov, R. Ludwig, Coupled microstrip line transverse electromagnetic resonator model for high-fied magnetic resonance imaging, Magn. Reson. Med. 47 (2002) 579–593.
[27] R.E. Collin, Field Theory of Guided Waves, second ed., IEEE Press, Piscataway, NJ, 1991, p. 459 ff.
[28] D. Landau, L. Lifschitz, Op. Cit., p. 291.
[29] R.D. Richtmeyer, Dielectric resonators, J. Appl. Phys. 10 (1939) 391–398.
[30] J. Tropp, A model for image shading in multi-mode resonators, in: Proceedings of the ISMRM, 2001, p. 1129.
[31] J. Tropp, E. Boskamp, US Patent 6,232,779, NMR RF coil with improved resonant tuning and field containment, 2001.
[32] J. Tropp, P. Calderon, Direct comparison of transmit efficiency in bird-cage and TEM resonators, in: Proceedings of the International Society of Magnetic Resonance in Medicine, 2001, p. 1119.
[33] J. Tropp, Dissipation, resistance, and rational impedance matching for TEM and birdcage resonators, Magn. Reson. Eng. B 15 (2002) 177.
[34] D.K. Spence, S.M. Wright, 2-D full wave solution for the analysis and design of birdcage coils, Magn. Reson. Eng. B 18 (2003) 15–23.
[35] L. Pincherle, Electromagnetic waves in metal tubes filled longitudinally with two dielectrics, Phys. Rev. 66 (1944) 118–130.
[36] W.R. Smythe, Op. Cit., Chapter IV.
[37] M. Abramowitz, I. Stegun (Eds.), Handbook of Mathematical Functions, Dover Publications, New York, 1972, Chapter 10.
[38] J.A. Stratton, Electromagnetic Theory, McGraw Hill, New York, 1941, p. 237.